ACS Sustainable Chemistry & Engineering

Research Article

Cite This: ACS Sustainable Chem. Eng. 2019, 7, 12464−12473

pubs.acs.org/journal/ascecg

# Role of the Structure of Graphene Oxide Sheets on the $CO_2$ Adsorption Properties of Nanocomposites Based on Graphene Oxide and Polyaniline or $Fe_3O_4$-Nanoparticles

S. Rodríguez-García,[†] R. Santiago,[‡] D. López-Díaz,[†] M. D. Merchán,*[,†] M. M. Velázquez,[†] J. L. G. Fierro,[§] and J. Palomar[‡]

[†]Departamento de Química Física, Facultad de Ciencias Químicas, Universidad de Salamanca, E-37008 Salamanca, Spain

[‡]Departamento de Ingeniería Química, Universidad Autónoma de Madrid, 28049 Madrid, Spain

[§]Instituto de Catálisis y Petroleoquímica, CSIC, 28049 Cantoblanco, Madrid, Spain

Supporting Information

**ABSTRACT:** New nanocomposites based on graphene oxide with polyaniline (PANI) or $Fe_3O_4$ nanoparticles (MG) were synthesized for $CO_2$ capture. To study the effect of graphene oxide structure on the $CO_2$ retention capacity, $CO_2/N_2$ selectivity, adsorbent regeneration, and adsorption kinetics, two different graphene oxides were synthesized by oxidation of graphite flakes (GO) and commercial carbon nanofibers (NSGO). $CO_2$ adsorption isotherms at 300 K were evaluated by gravimetric experiments. The results described the $CO_2$ adsorption as reversible physisorption mechanism, where the $CO_2$ adsorption capacity increases linearly with the micropore volume. Results also demonstrate the good $CO_2/N_2$ selectivity, recyclability, and fast adsorption kinetics of the materials tested. Differences concerning the adsorption properties of nanocomposites are related to the chemical composition and the size of graphene oxide sheets.

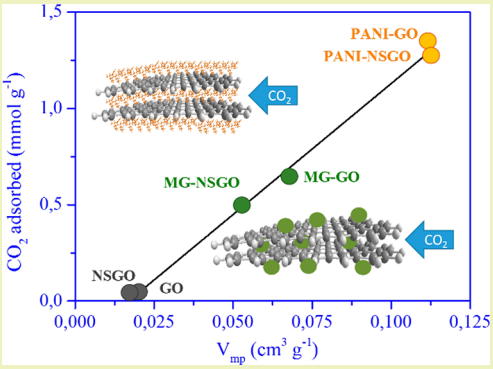


**KEYWORDS:** *Graphene oxide, Polyaniline, Iron oxide nanoparticles, Carbon dioxide, Adsorption*

## INTRODUCTION

Global warming constitutes a serious problem for the planet. The increase in the concentration of greenhouse gases, especially $CO_2$, makes it necessary to develop processes for its elimination.[1,2] The increase in the $CO_2$ emissions in the last 20 years was analyzed in an interesting review recently published.[2] The authors proposed a reduction of the annual rate of growth emission until 1.4%, lower than the average rate during the period of 1970−2000. Research has been focused on improving the current $CO_2$ capture and storage technologies to mitigate the $CO_2$ effectively and economically.[3] Different kinds of $CO_2$-capturing methodologies have been developed taking into account the effluent and concentration of the gas to be captured.[4] In this sense, membrane purification, adsorption, and absorption operations have been widely studied.[3,4] The chemical absorption in liquid amines is one of the most extensively used ones.[5,6] However, this methodology possesses several disadvantages, such as equipment corrosion[7,8] and low energy efficiency due to the high temperatures used in the desorption process.[9] For this reason, adsorption operation is preferred. In addition, for an efficient cyclic use, physisorption mechanism drives to better results.[9−11] Zeolites or active carbons have been widely studied, showing high capacity to retain $CO_2$; however, the selectivity toward $CO_2$ retention is very low.[12−14] This is mainly due to their high specific surface area, despite the fact that the $CO_2$ adsorption depends not only on the pore concentration and structure but also on the surface chemistry nature.[15] Other promising solid materials are metal−organic frameworks (MOFs) also widely investigated as $CO_2$ adsorbents due to their inherent adaptability of their chemistry and porous structure.[16]

Recently, preparation of hybrid composites based on carbonaceous materials, including active carbons, graphite, and graphene, seems to be a promising method to keep exploring.[14,15,17] Several strategies such as the structure and morphology control using hydrogels and aerogels,[18,19] nanospheres,[20,21] and nanotubes[17] through optimization of the composition via cation exchange,[18] surface modification, or nitrogen-based[22−27] or metal-based[28] functionalization have been investigated. The functionalization of graphene has proved to be a good strategy to improve the $CO_2$ adsorption capacity.[29−33] Thus, graphene functionalization with polyaniline increases the degree of recyclability and the $CO_2$ adsorption capacity between three and four times at high pressures[29] compared with pristine graphene,[34] while function-

Received: April 11, 2019
Revised: June 4, 2019
Published: June 24, 2019






DOI: 10.1021/acssuschemeng.9b02035
ACS Sustainable Chem. Eng. 2019, 7, 12464−12473

alization with $Fe_3O_4$ nanoparticles increases three times the $CO_2$ capture capacity.[30]

Despite the good results previously described, research should focus on improving simultaneously the $CO_2$ retention, selectivity, adsorption rate, and recyclability[11] and using materials and processes economically profitable and sustainable as well. Since nanocomposites based on graphene seem to be good $CO_2$ adsorbents, we expect that the replacement of graphene by graphene oxide could drive to new materials with modulated properties to achieve high $CO_2$ retention capacity and simultaneously high $CO_2$ selectivity, fast $CO_2$ adsorption, and easy recyclability.[35−38]

The main contribution of this paper is to explore the replacement of graphene by graphene oxide avoiding the reduction stages with hydrazine and chemical activation treatments in nanocomposites prepared with polyaniline or $Fe_3O_4$ nanoparticles directed to be used as $CO_2$ adsorbents. The presence of O groups in graphene oxide allows one to modulate the chemical composition in the surface by joining different types of materials resulting in new nanocomposites. The second objective of the paper is to know the role of graphene oxide on the capacity, selectivity, recyclability, and kinetics of the $CO_2$ retention process. This is the first time that $CO_2$ retention capacity is analyzed in terms of the structural properties of graphene oxide. The materials selected to synthesize graphene oxides were graphite flakes (GO) and carbon nanofibers (NSGO) because we demonstrated[36] that they contain different chemical composition, superficial charge density, and nanoplatelet size. We used as the second component polyaniline copolymerized from aniline in the presence of graphene oxide[29,39] and $Fe_3O_4$ nanoparticles.[40−42]

Exhaustive characterization of the starting graphene oxides and the nanocomposites allows us to obtain some main insights on how to modify the graphene oxide structure and the nature of the second component for modulating and improving their $CO_2$ adsorbent behavior. The strategy proposed is based on the previously known characteristics of graphene oxide sheets, very different, resulting in composite materials with different adsorption capacities.

## EXPERIMENTAL SECTION

**Chemical and Materials.** To synthesize graphene oxides with different chemical composition, we oxidized natural graphite flakes (99.02%) of fixed carbon, from Qingdao Super Graphite Co., Ltd., and GANF helical-ribbon carbon nanofibers non-graphitized provided by Carbon Advanced Materials, Grupo Antolín (Burgos, Spain).

Reagents $NaNO_3$ (99%), $H_2SO_4$ (98% wt), $KMnO_4$ (>99%), $H_2O_2$ (30% wt), NaOH, HCl (35%), and aniline were provided by Sigma-Aldrich (St. Louis, MO). $FeCl_3{\cdot}6H_2O$ and $FeSO_4{\cdot}7H_2O$ were supplied by Panreac Química SLU (Barcelona, Spain). All reagents were used without purification. Millipore Ultrapure water was obtained by combination of RiOs and Milli-Q systems from Millipore.

Carbon dioxide ($CO_2$), nitrogen ($N_2$), and helium (He) were supplied by Praxair Inc. and oxygen ($O_2$) by L'Air Liquide, Madrid, Spain. The minimum purity > 99.999%.

**Synthesis of Polyaniline-Graphene Oxide Nanocomposites.** Prior to synthesizing polymer−graphene oxide nanocomposites, we synthesized graphene oxides with different structure by oxidizing graphite flakes and carbon nanofibers GANF with a modified Hummers method.[35,36,38]

The polyaniline-GO (PANI−GO) and polyaniline-NSGO (PANI−NSGO) nanocomposites were synthesized by in situ polymerization procedures previously reported.[39,43] Briefly, aniline was added to graphene oxide dispersions of 2 mg/mL. The GO:aniline mass ratio used in all experiments was 15:85.[39] The graphene oxide dispersions prepared by sonication for 1 h in 15 min cycles were mixed with aniline and sonicated for 1 h (15 min cycles). The polymerization was performed under stirring by carefully addition of 6 mL of $H_2O_2$ (30%), 4.5 mL of HCl (37%) and 1 mL of $FeCl_3.6H_2O$ (0.1 M).[43] The total volume was fixed in 200 mL with ultrapure water. The suspension was maintained under stirring at 273 K for 24 h; to improve the performance of the reaction after that it was kept at room temperature for 5 h. To remove the unreacted polyaniline, nanocomposites were separated by filtration and carefully washed with 0.1 M HCl until the filtrate was completely transparent. Finally, the solids were washed with acetone to eliminate the excess of graphene oxide and dried at 333 K under vacuum for 24 h. Nanocomposites were thermally activated at 700 °C under inert gas in a tubular furnace for 1 h.[39]

**Synthesis of $Fe_3O_4$ Nanoparticles and Graphene Oxide Nanocomposites.** Functionalization of the graphene oxides with $Fe_3O_4$ nanoparticles was carried out by a procedure previously reported.[44] A 200 mL amount of GO or NSGO solutions (1 mg/mL) was heated to 363 K; then we added 20 mL of 0.2 M $FeCl_3{\cdot}6H_2O$, 10 mL 0.2 M of $FeSO_4{\cdot}7H_2O$, and 38.4 mL of $NH_4OH$. The solution was stirred at 363 K for 30 min and then cooled down to room temperature. The precipitate was separated by filtration, washed twice with 200 mL of $H_2O$, and dried at 343 K for 24 h.

**Structural Characterization.** XPS of powder samples was measured in a VG Escalab 200R spectrometer (Fisons Instruments) equipped with an excitation source of Mg K$\alpha$ ($h\nu$ = 1253.6 eV) radiation and a hemispherical electron analyzer. High-resolution spectra were recorded at a 50 eV analyzer pass energy. The residual pressure in the analysis chamber was maintained under $4 \times 10^{-7}$ Pa during data acquisition. FTIR spectra were recorded in a Vertex 70v spectrometer from Bruker operating in vacuum. It is equipped with a LN2 detector working with a nominal resolution of 0.2 $cm^{-1}$. Samples were pressed in KBr (Merck) pellets with a hybrid/KBr mass ratio of 1:300. Thirty scans were recorded to improve the signal-to-noise ratio.

Powder XRD patterns were recorded in a Bruker D8 Advance powder diffractometer using Cu K$\alpha_{1,2}$ radiation ($\lambda$ = 1.54050 Å) between 10° and 80° (2$\theta$) with a step size of 0.05° and a step time of 2.6 s. The tube was operated at 40 kV and 30 mA.

Scanning electron microscopy (SEM) images were taken in a Hitachi S-3000N microscope with an accelerating voltage of 5 kV. SEM samples were mounted on a stub of gold (40−60 nm) with adhesive. Transmission electron microscopy (TEM) images of $Fe_3O_4$ nanocomposites were taken with a 120 kV Tecnai G2 Spirit TWIN from FEI. Nanocomposite films were deposited on Formvar-carbon-coated copper grid by the drop casting methodology.

The porous structure was revealed by the 77 K $N_2$ adsorption/desorption isotherms in the relative pressure range from 0 to 1 in a TriStar II 3020 (Micromeritics) system after degasification at 0.1 mbar and 423 K conditions for at least 12 h. The surface area was calculated with the BET equation within the range of relative pressure $0.05 < P/P_0 < 0.30$.

Narrow microporosity of nanocomposites was evaluated by the $CO_2$ adsorption isotherms at 273 K in the relative pressure range from 0 to 0.03 in the TriStar II 3030 (micromeritics). The micropore volume was calculated attending to the Dubinin−Radushkevich model.[45]

Thermal gravimetric analyses (TGA) were performed on a SDT Q600 apparatus (TA Instruments, Madrid, Spain) under a flow of 20 mL/min of oxygen and a heating rate of 15 K/min from room temperature to 1173 K.

**$CO_2$ Adsorption Gravimetric Measurements.** We used a high-pressure sorption analyzer (ISOSORP GAS LP-flow, Rubotherm) with a magnetic suspension balance (MSB) to measure the $CO_2$ and $N_2$ adsorption capacities (mmol/g). The balance covers a weight range up to 10 g with a precision of $10^{-5}$ g. In addition, it can operate in a wide range of temperatures (from room temperature to 150 °C) and pressures (from $10^{-3}$ mbar to 25 bar). The buoyancy effect was corrected before the adsorption experiments by using an inert gas (He). He gas is flowed through the sample (from 1 to 20 bar) after



DOI: 10.1021/acssuschemeng.9b02035
ACS Sustainable Chem. Eng. 2019, 7, 12464−12473

**Table 1. Values of Binding Energies and Percentages of Different Groups for Nanocomposites with Polyaniline Obtained from XPS Measurements**

| sample | C 1s emission | max. binding energy (eV) | atomic composition (%) | N 1s emission | max. binding energy (eV) | atomic composition (%) |
|---|---|---|---|---|---|---|
| GO[a] | C═C | 284.8 | 51 ± 3 | | | |
| | C−O | 286.4 | 42 ± 2 | | | |
| | COOH | 287.9 | 7 ± 0.4 | | | |
| NSGO[a] | C═C | 284.8 | 42 ± 2 | | | |
| | C−O | 286.4 | 44 ± 2 | | | |
| | COOH | 288.4 | 14 ± 1 | | | |
| PANI−GO | C═C | 284.6 | 64 ± 4 | ═N | 398.3 | 32 ± 2 |
| | C−N | 285.6 | 20 ± 1 | −N | 399.4 | 19 ± 1 |
| | C−O | 286.7 | 12 ± 0.5 | $-N^+$ | 400.7 | 39 ± 2 |
| | COOH | 288.0 | 4 ± 0.2 | $=N^+$ | 402.3 | 10 ± 0.8 |
| PANI−NSGO | C═C | 284.7 | 69 ± 4 | ═N | 398.3 | 33 ± 2 |
| | C−N | 285.6 | 13 ± 0.8 | −N | 399.4 | 13 ± 1 |
| | C−O | 286.7 | 14 ± 0.8 | $-N^+$ | 400.7 | 43 ± 2 |
| | COOH | 288.0 | 4 ± 0.2 | $=N^+$ | 402.3 | 11 ± 0.7 |

[a]Data taken from ref 36.

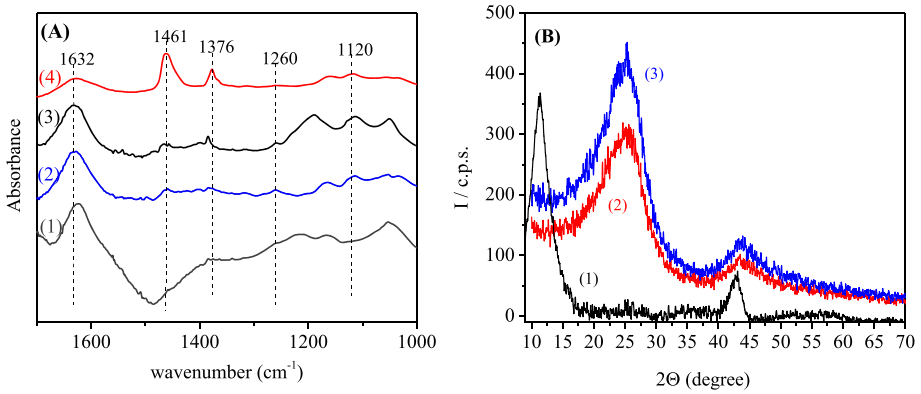


**Figure 1.** (A) FTIR spectra of PANI−graphene oxide nanocomposites: NSGO (line 1), PANI−NSGO (line 2), GO (line 3), and PANI−GO (line 4). (B) X-ray diffractograms of GO and NSGO (line 1), PANI−GO (line 2) and PANI−NSGO (line 3). For the sake of clarity, spectra were vertically shifted.

degasification at $10^{-3}$ mbar and 333 K. $CO_2$ and $N_2$ adsorption isotherms were performed at 300 K. The estimated uncertainties ($u$) of equilibrium measurements are $u(P)$ = 0.01 bar, $u(T)$ = 0.1 K, and $u$(adsorption capacity) = 0.002 mmol·g$^{-1}$. The reversibility of the $CO_2$ desorption process was tested by pressure swing. The volume gas flow fed through the loaded sample (100−150 mg) was 100 N mL/min.[46] After the $CO_2$ and $N_2$ adsorption, the equipment records the mass gained at each time, which has to be corrected. The sample is considered totally saturated when the weight change is less than 0.02 mg/h. The amount of $CO_2$ or $N_2$ adsorbed, $q_e$ is quantified in terms of millimoles of $N_2$ or $CO_2$ per mass of the adsorbent material after degasification: $q_e = (m/M)/m_{material}$.

We calculate the $CO_2$ selectivity using the ideal adsorbed solution (IAS) method[11,47]

$$\alpha_{CO_2/N_2} = \frac{q_{CO_2}/q_{N_2}}{p_{CO_2}/p_{N_2}} \quad (1)$$

where $\alpha_{CO2/N2}$ is the $CO_2$ selectivity and $q_{CO2}$ and $q_{N2}$ represent the adsorption capacities (mmol/g) of $CO_2$ and $N_2$, respectively, obtained from the gas−solid isotherms at the corresponding $CO_2$ and $N_2$ partial pressures $p_{CO2}$ and $p_{N2}$.

The mass transfer kinetic of the gas−solid adsorption was quantified by means of a pseudo-second-order model, reported by Ho and McKay,[48] successfully applied to heterogeneous adsorbents in previous works[49,50] and described by the following linear equation

$$\frac{t}{q_t} = \frac{1}{K_2 \cdot q_e^2} + \frac{t}{q_e} \quad (2)$$

where $q_t$ and $q_e$ are the adsorbent capacity at each time ($t$) and at the equilibrium respectively (mmol/g) and $K_2$ represents the pseudo-second-order kinetic adsorption constant (g/mmol·min).

## RESULTS AND DISCUSSION

**Chemical Characterization of Polyaniline−Graphene Oxide Nanocomposites.** The C 1s core-level spectra are plotted in Figures S1 and S2 of the SI. Spectra present asymmetric lines that can be fitted to three functions. Table 1 collects the binding energy values of each component. The percentage of each component is calculated from the resulting area. For comparison, data corresponding to graphene oxides (GO) and (NSGO)[36] are also in Table 1.

Results in Table 1 show the three components of C 1s emission for neat graphene oxides centered at 284.8, 286.4, and 287.9 eV. These peaks were previously assigned[51] to C−C bonds in aromatic networks, to C−O bonds in alcohol or epoxy groups, and to $COO^-$ groups, respectively.[36,52] The percentage of functional groups depends on the nature of the starting material. In PANI nanocomposites a fourth peak centered at 285.6 eV is assigned to the C−N bond.[53] Besides, a new band ascribed to the N 1s core-level spectrum also appears (see Figure S2 of the SI). The N 1s spectrum is an asymmetric


DOI: 10.1021/acssuschemeng.9b02035
ACS Sustainable Chem. Eng. 2019, 7, 12464−12473

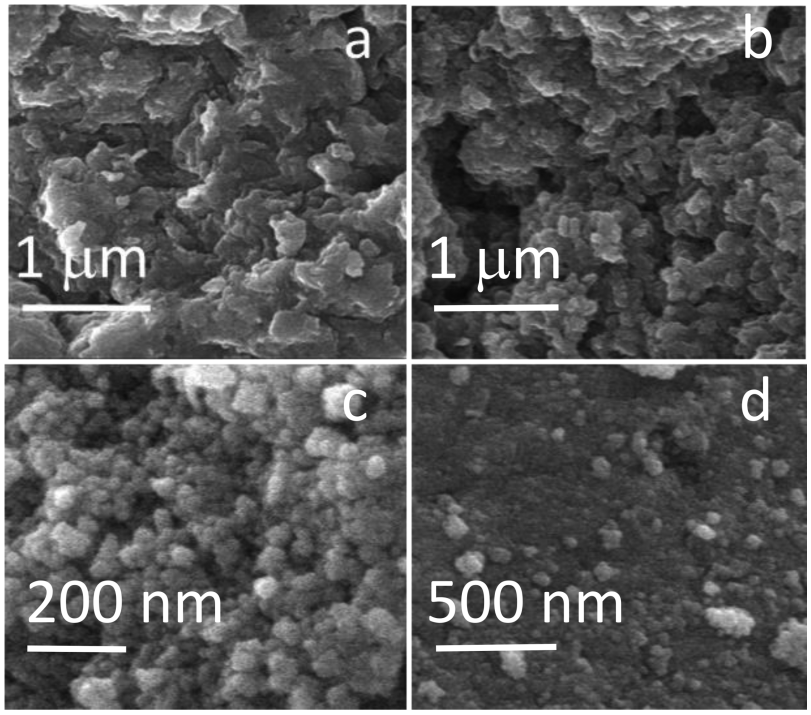


**Figure 2.** SEM images of (a) PANI−GO, (b) PANI−NSGO, (c) MG−GO, and (d) MG−NSGO.

**Table 2. Values of Binding Energies and Percentages of Different Groups for Nanocomposites with $Fe_3O_4$ Nanoparticles Obtained from XPS Measurements**

| sample | C 1s emission | max. binding energy (eV) | atomic composition (%) | O 1s emission | max. binding energy (eV) | composition (%) |
|---|---|---|---|---|---|---|
| GO[a] | C═C | 284.8 | 51 ± 3 | C═O | 531.2 | 16 ± 0.8 |
| | C−O | 286.4 | 42 ± 2 | C−O | 532.7 | 66 ± 3 |
| | COOH | 287.9 | 7 ± 0.4 | O−H | 533.4 | 17 ± 0.7 |
| NSGO[a] | C═C | 284.8 | 42 ± 2 | C═O | 531.2 | 31 ± 2 |
| | C−O | 286.4 | 44 ± 2 | C−O | 532.7 | 52 ± 3 |
| | COOH | 288.4 | 14 ± 1 | O−H | 533.4 | 17 ± 1 |
| MG−GO | C═C | 284.8 | 76 ± 4 | O−Fe | 530.1 | 65 ± 3 |
| | C−O | 286.2 | 18 ± 1 | C═O | 531.6 | 25 ± 1 |
| | COOH | 287.7 | 6 ± 3 | C−O | 532.6 | 9 ± 0.8 |
| | | | | O−H | 533.8 | 1 ± 0.5 |
| MG−NSGO | C═C | 284.8 | 68 ± 4 | O−Fe | 530.1 | 67 ± 3 |
| | C−O | 286.2 | 23 ± 1 | C═O | 531.6 | 23 ± 1 |
| | COOH | 287.7 | 9 ± 2 | C−O | 532.6 | 9 ± 0.6 |
| | | | | O−H | 533.8 | 1 ± 0.4 |

[a]Data taken from ref 36.

band that fits acceptably to four functions centered at 398.3, 399.4, 400.7, and 402.3 eV. The position and percentage of the different groups are collected in Table 1. These peaks were previously observed for polyanilines and ascribed to imine, amine, charged amine, and charged imine moieties respectively.[54] Data in Table 1 clearly show that the main difference between the composites is the percentage of −N and $-N^+$: 19% and 39% for PANI−GO and 13% and 43% for PANI−NSGO. The appearance of the N 1s spectrum characteristic of polyaniline and the peak of C−N bonds in C 1s core-level spectra unequivocally demonstrates formation of hybrid materials between graphene oxides and PANI. Besides, the percentage of both C−O and COOH groups in nanocomposites decreases compared with those of graphene oxides. This fact evidences that the interactions between graphene oxides and PANI are through those functional groups. Simultaneously, the percentage of $C_{sp^2}$ increases after functionalization due to the aromatic groups of PANI. This is an additional argument to prove the functionalization of graphene oxides with the polymer PANI.

The chemical composition was also analyzed recording the FTIR spectra of polyaniline−graphene oxide nanocomposites. Spectra are collected in Figure 1A.

Bands centered at 1632, 1461, and 1376 $cm^{-1}$ in Figure 1A are assigned to the stretching of aromatic C═C, N═N, and C−N bonds, respectively. The peak centered at 1632 $cm^{-1}$ confirms the existence of aromatic groups of graphene oxide in nanocomposites, while bands assigned to N═N and C−N bonds indicate the presence of imine and amine groups[55] in nanocomposites detected by XPS. Peaks centered at 1260 and 1120 $cm^{-1}$ are assigned to the stretching of protonated amine and imine groups, respectively,[56−58] produced during the



DOI: 10.1021/acssuschemeng.9b02035
ACS Sustainable Chem. Eng. 2019, 7, 12464−12473

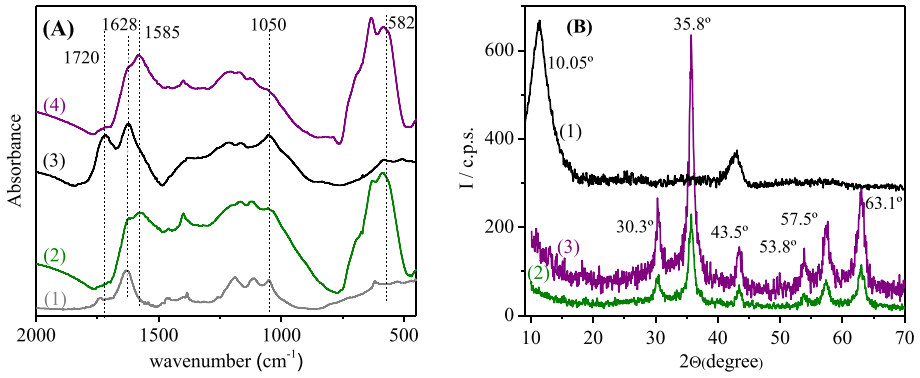


**Figure 3.** (A) FTIR spectra of MG−graphene oxide nanocomposites: GO (line 1), MG−GO (line 2), NSGO (line3), and MG−NSGO (line 4). (B) X-ray diffractogram of GO and NSGO (line 1), MG−GO (line 2), and MG−NSGO (line 3). For the sake of clarity, spectra and the diffractogram of GO in Figure 3B are vertically shifted.

**Table 3. Pore Structure Parameters Obtained by the Dubinin−Radushkevich Model**[a]

| | GO | MG−GO | PANI−GO | NSGO | MG−NSGO | PANI−NSGO |
|---|---|---|---|---|---|---|
| $A_{BET}$ ($m^2/g$) | <5 | 157 | <5 | <5 | 248 | 42 |
| $V_{mp}$ ($cm^3/g$) | 0.020 | 0.068 | 0.112 | 0.018 | 0.053 | 0.113 |
| $E_0$ (kJ/mol) | 5.4 | 10.3 | 11.4 | 7.0 | 10.9 | 11.4 |
| $q_e$ (mmol/g) | 0.039 | 0.643 | 1.35 | 0.038 | 0.495 | 1.275 |
| $K_2$ (g/mmol·min) | 8.20 | 1.28 | 0.04 | 7.41 | 3.45 | 0.05 |

[a]Thermodynamic and kinetic parameters obtained by fitting the $CO_2$ kinetic adsorption curves (300 K and $p_{CO2}$= 1 bar) to eq 2.

synthesis at the acidic medium. In summary, the FTIR and XPS results show the presence of polyaniline groups on the nanocomposites.

An important property of layered solids with potential applications in gas adsorption is the interlayer structure. Therefore, we recorded the X-ray diffractograms (XRD) of materials (Figure 1B) to study the effect of functionalization on the interlayer distance of graphene oxides layers.

Diffractograms of graphene oxide synthesized from graphite (GO) and from carbon nanofibers (NSGO) are quite similar. Therefore, Figure 1B represents the diffractogram of GO. It presents two characteristics peaks at 10.05° and 42.90°. The interlayer distance value calculated from Bragg's law was 0. 43 nm, in excellent agreement with data in the literature.[59−61] Diffractograms of nanocomposites present a new peak at 26° assigned to the (200) crystal plane of PANI.[62] Moreover, the diffraction peak of graphene oxide disappears. This fact was previously reported and attributed to the GO exfoliation during the polymerization process of aniline.[62]

Figure 2a and 2b shows the surface morphology of PANI−GO and PANI−NSGO obtained by SEM. Images display PANI covering the nanocomposite without apparent mesopore or macropore signs.

**Chemical Characterization of $Fe_3O_4$ Nanoparticles−Graphene Oxide Nanocomposites.** Figures S3 and S4 of the SI collect the C 1s and O 1s core-level spectra of $Fe_3O_4$ nanoparticles−graphene oxide nanocomposites. The C 1s core-level spectrum is an asymmetric peak that fits to three components. The O 1s spectra of nanocomposites fits to four peaks, while three components are good enough to interpret the O 1s core-level spectra of graphene oxides. Table 2 collects the maximum position and the percentage of the different species.

Results in Table 2 show that the O 1s peak of neat graphene oxides can be fitted to three components centered at 531.2, 532.7, and 533.4 eV. These peaks were previously reported[63] and assigned to C═O, C−O, and OH bonds in $COO^-$ groups, respectively. After functionalization with $Fe_3O_4$ nanoparticles, XPS results show a sharp decrease on the percentage of C−O and O−H and a new peak at 530.1 eV assigned to O−Fe bonds.[64,65] Accordingly, XPS results indicate that the $Fe_3O_4$ nanoparticles grafted onto graphene oxide sheets through O−Fe bonds of epoxy groups. Finally, the Fe 2p XPS spectra of the nanocomposites (see Figure S5 of the SI) exhibit two peaks at 711.2 and 725.1 eV corresponding to Fe $2p_{3/2}$ and Fe $2p_{1/2,}$ respectively,[66−68] the asymmetric band centered at around 711 eV, and the satellite peak at 719.5 eV, revealing the existence of $\gamma$-$Fe_2O_3$.[67] From XPS results we conclude that the synthesis method drives to nanocomposites of graphene oxides and $Fe_3O_4$ nanoparticles. Figure 2c and 2d shows the surface morphology of MG−GO and MG−NSGO, respectively; the SEM images display a nearly uniform distribution of $Fe_3O_4$ on the surface. TEM images of MG−GO and NSGO (Figure S6 of the SI) were presented to determine the size of $Fe_3O_4$ nanoparticles. TEM images clearly show graphene oxide sheets coated with $Fe_3O_4$ nanoparticles of diameter around 10 nm.

The FTIR spectra of $Fe_3O_4$ nanocomposites are depicted in Figure 3A. As can be seen in Figure 3A, the most important change after functionalization with $Fe_3O_4$ is the new band located at 582 $cm^{-1}$ assigned to the stretching vibration of O−Fe bonds.[69] On the other hand, a significant decrease of the intensity of the C═O and C−O bands at 1720 and 1050 $cm^{-1}$ is observed. A new band centered at 1585 $cm^{-1}$ appeared in the FTIR spectrum after functionalization. This band has been previously reported and assigned to bonds between carboxylate head and metal atom.[70] All results evidence the formation of bonds between different O groups of graphene oxides and iron atoms of $Fe_3O_4$ nanoparticles.

X-ray diffractograms of nanocomposites of graphene oxides and $Fe_3O_4$ present new peaks centered at 30.3°, 35.8°, 43.5°, 53.8°, 57.8°, and 63.1°, Figure 3B. These peaks were assigned


DOI: 10.1021/acssuschemeng.9b02035
ACS Sustainable Chem. Eng. 2019, 7, 12464−12473

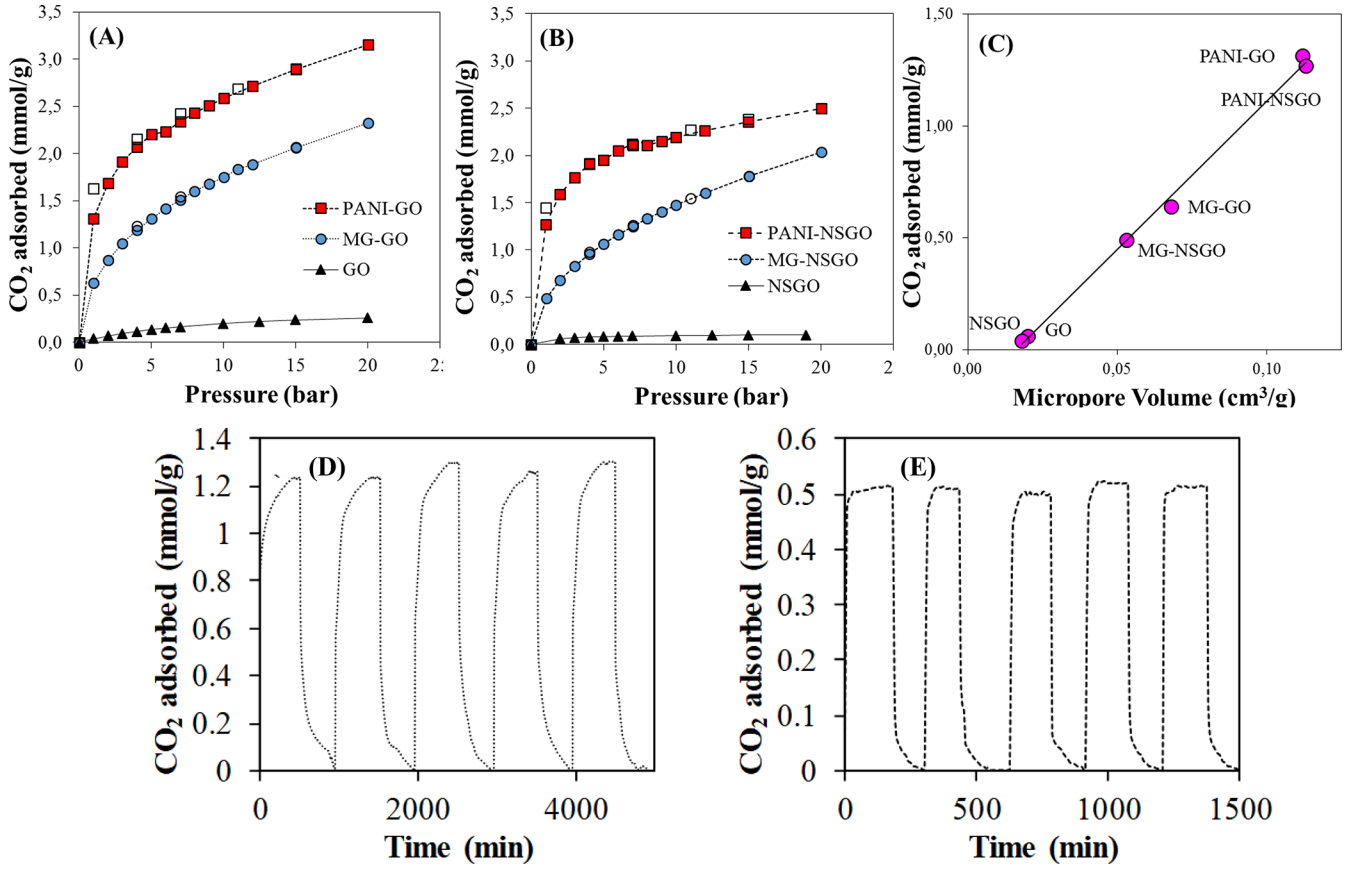


**Figure 4.** (A and B) Adsorption isotherms of $CO_2$ in nanocomposites based on (A) (GO) and (B) (NSGO) at 300 K. Filled symbols represent the pressure increase and empty symbols the pressure decrease. Lines are visual guides. (C) Variation of the $CO_2$ adsorbed on nanocomposites at 1 bar of $CO_2$ partial pressure and 300 K. Solid line corresponds to linear fit of the experimental data. (D and E) Cycles of $CO_2$ adsorption (303 K and 1 bar of $CO_2$ partial pressure) and desorption (333 K and 1 bar of $N_2$ partial pressure) for (D) PANI−GO and (E) MG−NSGO.

to (220), (331), (400), (422), (511), and (440) reflections of the pure cubic spinel crystal structure of $Fe_3O_4$ nanoparticles.[64] In summary, XPS, FTIR, and XRD results confirm the functionalization of graphene oxides with $Fe_3O_4$ nanoparticles and demonstrate the interactions between components through the O−Fe bonds.

**Porous Structure.** The surface area and micropore volume of materials were obtained from the adsorption−desorption isotherms of $N_2$ (77 K) and $CO_2$ (273 K), respectively (see Figure S7 of the SI). Table 3 shows the surface area ($A_{BET}$) values calculated from $N_2$ adsorption isotherms and the BET equation. The micropore volume ($V_{mp}$) and the characteristic energy of adsorption ($E_0$) values calculated from $CO_2$ isotherms and the Dubinin−Radushkevich model are shown in Table 3. See details in section 2 and Figure S8 of the SI.

Table 3 clearly shows that graphene oxides, GO and NSGO, present low values of surface area ($A_{BET}$) and micropore volume ($V_{mp}$), which may anticipate a low $CO_2$ retention capacity. However, functionalization with PANI or $Fe_3O_4$ nanoparticles significantly increases the porosity and micropore volume of graphene oxides. Results in Table 3 also show that the micropore volume is significantly higher for PANI−nanocomposites than for the $Fe_3O_4$. This behavior is expected since polymers highly functionalized with amine and/or $\pi$-conjugated bonds render high micropore volume.[71,72]

It is also important to notice that $V_{mp}$ values increase after functionalization: 82% for PANI−GO, 84% for PANI−NSGO, 70% for MG−GO, and 66% for MG−NSGO. On the other hand, the low values found for the adsorption energy values (5−12 kJ/mol) suggest a physisorption mechanism for all nanocomposites.[73] Results in Figure S9 of the SI indicates that the distribution of pore diameter for PANI nanocomposites is almost independent of graphene oxide structure, while small differences are detected for $Fe_3O_4$ nanocomposites above 8 Å.

**$CO_2$ Adsorption in Prepared Nanocomposites.** Figure 4A and 4B presents the $CO_2$ isotherms of the nanocomposites and the benchmark graphene oxides (GO and NSGO) measured by gravimetric analysis at 300 K and the pressure range of 1−20 bar. As can be seen graphene oxides obtained from graphite (GO) and carbon nanofibers (NSGO) present a low amount of $CO_2$ adsorbed at different pressure conditions, in good agreement with their low surface area and almost null microporosity. However, functionalization with $Fe_3O_4$ nanoparticles increases the total amount of adsorbed $CO_2$ to reach 2.3 mmol/g for MG−GO and 2.0 mmol/g for MG−NSGO at 20 bar of pressure. Finally, incorporation of polyaniline in graphene oxides sheets further increases the $CO_2$ adsorption capacity until 3.2 mmol/g for PANI−GO and to 2.5 mmol/g for PANI−NSGO nanocomposites at 20 bar of $CO_2$. From our results, the capacity of nanomaterials to capture $CO_2$ increases as follows: PANI−GO > PANI−NSGO > MG−GO > MG−NSGO > GO > NSGO.

If we analyze the ratio between the $CO_2$ retention capacities of nanocomposites compared to pure graphene oxide, we find that for MG−NSGO and PANI−NSGO it is, respectively, 20 and 25 times the $CO_2$ adsorption capacity of NSGO (from 0.1


DOI: 10.1021/acssuschemeng.9b02035
ACS Sustainable Chem. Eng. 2019, 7, 12464−12473

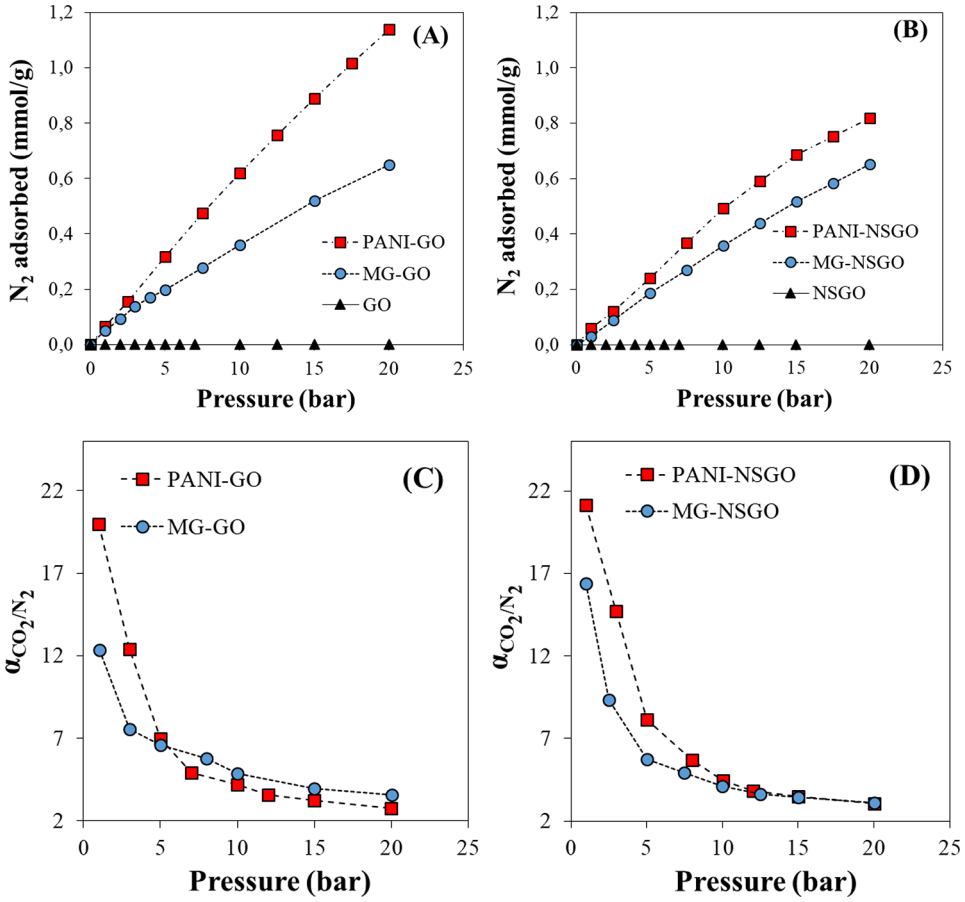


**Figure 5.** (A and B) Adsorption isotherms of $N_2$ in nanocomposites based on (A) graphite(GO) and (B) (NSGO) at 300 K. (C and D) Variation of $CO_2/N_2$ selectivity with pressure at 300 K for nanocomposites based on (C) graphite (GO) and (D) carbon nanofibers (NSGO). Lines are visual guides.

mmol/g NSGO to 2.0 and 2.5 mmol/g for MG−NSGO and PANI−NSGO, respectively). These ratios are somewhat lower for MG−GO and PANI−GO, 9.2 and 12.8 times, respectively, the $CO_2$ uptake of GO (from 0.25 mmol/g for GO to 2.3 and 3.2 mmol/g for MG−GO and PANI−GO, respectively) but in any case much higher than the increase of 3 or 4 times presented in the literature for graphene composites.[29,30]

We analyzed the micropore volume dependence of the $CO_2$ adsorption capacity in Figure 4C. Results show a nearly linear dependence between the $CO_2$ adsorption capacity (measured at 1 bar) and the micropore volume corresponding to micropores with pore diameter values below 15 Å. Similar linear dependence was previously reported[10] in gas adsorption by adsorbents with pores diameter < 15 Å. This condition is fulfilled in all of our systems, as indicated from analysis of the pore diameter distribution (Figure S9 of SI). Therefore, our results prove that the nanocomposites of graphene oxides with $Fe_3O_4$ nanoparticles or polyaniline drives to an increase of the micropore volume, which seems to be responsible for the increase of the $CO_2$ adsorption capacity. The low values (5−12 kJ/mol) of characteristic adsorption energy ($E_0$ collected in Table 3), the easily exhausted adsorbent regeneration (white symbols in Figure 4A and 4B), and the adsorption capacity−micropore volume linear relationship (Figure 4C) indicate that the $CO_2$ adsorption on tuned graphene oxides with PANI and $Fe_3O_4$ is mainly driven by a physisorption mechanism.

Looking at the role of the graphene oxide sheets, when the second component is polyaniline, composite with GO has a slightly higher $CO_2$ retention capacity than the composite with NSGO. In that case, these differences seem to be related to the higher functionalization degree of this composite. This major functionalization degree can be visualized by the higher percentage of C−N bonds obtained by XPS for composites based on GO than for composites prepared with NSGO. Taking into account that the total atomic contents of C/N/O are 87.6/6.4/6.0 for PANI−GO and 87.3/6.6/6.1 for PANI−NSGO, as the ratios N/C in both PANI composites are similar, we can say that the amount of C−N bonds is higher in PANI−GO than in PANI−NSGO. This behavior is likely due to the larger size of GO nanoplatelets, 825[36] against 106 nm NSGO.[36] Besides, the percentage of neutral amines (XPS) is higher for PANI−GO (19%) than for PANI−NSGO (13%) composites. This fact seems to providea higher micropore volume[71,72] and a greater basic character to GO composites favoring the $CO_2$ retention due.[23] In the case of nanocomposites with $Fe_3O_4$ nanoparticles, the micropore volume is slightly greater for MG−GO than for MG−NSGO. The atomic content of C/N/O/Fe in samples with $Fe_3O_4$ is MG−GO 31.9/2.0/48.1/18.0 and MG−NSGO 23.9/1.9/54.1/20.0. The ratio O/C is larger in $Fe_3O_4$ composites than in the composites with PANI, even subtracting the O atoms joined to Fe; we can say that these samples are more oxidized, which agrees with the lower micropore volume and slight enlargement of the pore sizes (see Figure S9 of SI).[74]

A main challenge in adsorbent design is to attain high $CO_2$ adsorption capacity (>2 mmol/g at $pCO_2$ = 0.15 bar).[11] The


DOI: 10.1021/acssuschemeng.9b02035
ACS Sustainable Chem. Eng. 2019, 7, 12464−12473

comparison to reported $CO_2$ adsorption capacity of common adsorbents at 1 bar of $CO_2$ partial pressure (see Table S1 in SI) describes the synthesized nanocomposites as $CO_2$ adsorbents with reasonable capacity (PANI−GO 1.31 mmol/g; PANI−NSGO 1.27 mmol/g) but still far from expected target value for an effective $CO_2$ sorbent.[11]

Concerning recyclability, we obtain the same gas uptake when the pressure is decreased (empty symbols in Figure 4A and 4B). This indicates that the $CO_2$ adsorption in these composites is a reversible process, which happens without loss of adsorption capacity. In addition, several cycles of $CO_2$ adsorption−desorption with nanocomposites were performed at 1 bar at 303 K for the adsorption and 333 K and a $N_2$ flow for the desorption. As can be seen in Figure 4 D and 4E, the $CO_2$ adsorption capacity of PANI−GO and MG−NSGO is preserved upon successive cycles; identical behavior is observed for all of the prepared nanocomposites. The efficient regeneration of exhausted adsorbents by pressure swing and stripping together with the high thermal stability (see the TGA curves in Figure S10 of the SI) indicates a favorable recyclability of the prepared nanocomposites in the $CO_2$ capture process.

An important aspect to evaluate in a suitable $CO_2$ adsorbent is the $CO_2/N_2$ selectivity. Therefore, we evaluate the $CO_2/N_2$ selectivity for all materials at 300 K by recording the $N_2$ adsorption isotherms at 300 K (Figure 5A and 5B) using eq 1 (IAST method by simulating bulk gas loading)[11] for the case of $p_{CO2} = p_{N2}$ in the range of studied pressures.

The $N_2$ adsorption capacity on nanocomposites follows a similar trend to that of $CO_2$ but with much lower $N_2$ uptakes than for $CO_2$. Figure 5C and 5D shows the variation of the $CO_2/N_2$ selectivity with the gas partial pressure. The $CO_2/N_2$ selectivity values are in the range of 2−21 almost independent of composition. This means that in all nanocomposites the $CO_2$ adsorption is selectively favored. Considering a more realistic scenario corresponding to a postcombustion flue gas ($p_{CO2}$ = 0.15 bar and $p_{N2}$ = 0.85 bar), the obtained IAST $CO_2/N_2$ selectivity values of prepared nanocomposites should be improved for an effective retention.[11]

Another important parameter in adsorption processes is the mass transfer rate. The rates of the gas−solid adsorption were evaluated by measuring the kinetic curves of $CO_2$ uptake in nanocomposites at 300 K and 1 bar (see Figure S11 in the SI). The kinetic curves were fitted to a pseudo-second-order model[48] (eq 2). Table 3 collects the best fitting parameters.

It is important to note that the adsorption capacity at equilibrium values ($q_e$) calculated from kinetic measurements and from the experimental equilibrium coincides with each other (see Figure S12 of the SI). On the other hand, our results show that the kinetic constant value, $K_2$, depends on the adsorbent and decreases as the micropore volume and adsorption capacity increases (see Figure S13 of the SI). This behavior is consistent with the effect of stronger mass transfer resistance in more microporous materials.[75] $K_2$ values for nanocomposites based on graphene oxides are higher than the values reported elsewhere for commercial $CO_2$ adsorbents at similar operating conditions.[50]

## CONCLUSIONS

We synthesized nanocomposites based on graphene oxides of different chemical composition with polyaniline or $Fe_3O_4$ nanoparticles for $CO_2$ retention. Our results demonstrated that the $CO_2$ adsorption capacity significantly increases with the micropore volume. Besides, the highest micropore volume is reached when graphene oxides are coated with the polymer PANI. We also proved that larger graphene oxide sheets favor the microporosity of the adsorbent and consequently increase the $CO_2$ retention. Finally, composites based on graphene oxides present good adsorption capacity and $CO_2/N_2$ selectivity, fast kinetics, and good thermal stability and recyclability according to the benchmark industrial checkpoints. On the other hand, our results proved that even though substitution of graphene by graphene oxide in nanocomposites does not improve the $CO_2$ adsorption capacity, it improves the recyclability of materials, avoiding the use of very high temperatures for cyclic use. Results also proved that it is possible to modulate the adsorption capacity of nanocomposites by modifying both the graphene oxide structure and the nature of the second component. This strategy can be presented as a good methodology to modulate efficient $CO_2$ adsorbents.

## ASSOCIATED CONTENT

### Supporting Information

The Supporting Information is available free of charge on the ACS Publications website at DOI: 10.1021/acssuschemeng.9b02035.

Details on the experimental section: characterization, porous structure, TGA, kinetic measurements (PDF)

## AUTHOR INFORMATION


### Corresponding Author

*Tel: +34 670 547 110. E-mail: mdm@usal.es.

### ORCID

R. Santiago: 0000-0002-6877-9001

M. D. Merchán: 0000-0003-3573-3805

M. M. Velázquez: 0000-0003-2746-8204

J. Palomar: 0000-0003-4304-0515


### Notes

The authors declare no competing financial interest.

## ACKNOWLEDGMENTS

Authors acknowledge financial support from the European Regional Development Fund (ERDF), Junta de Castilla y León (SA045U16 and SA256P18), and MINECO (CTQ2016-78895-R and CTQ2017-89441-R).

## REFERENCES


(1) Smol, J. P. Climate Change: A planet in flux. *Nature* **2012**, *483*, S12−S15.

(2) Mac Dowell, N.; Fennell, P. S.; Shah, N.; Maitland, G. C. The role of CO2 capture and utilization in mitigating climate change. *Nat. Clim. Change* **2017**, *7* (4), 243−249.

(3) Bui, M.; Adjiman, C. S.; Bardow, A.; Anthony, E. J.; Boston, A.; Brown, S.; Fennell, P. S.; Fuss, S.; Galindo, A.; Hackett, L. A.; Hallett, J. P.; Herzog, H. J.; Jackson, G.; Kemper, J.; Krevor, S.; Maitland, G. C.; Matuszewski, M.; Metcalfe, I. S.; Petit, C.; Puxty, G.; Reimer, J.; Reiner, D. M.; Rubin, E. S.; Scott, S. A.; Shah, N.; Smit, B.; Trusler, J. P. M.; Webley, P.; Wilcox, J.; Mac Dowell, N. Carbon capture and storage (CCS): the way forward. *Energy Environ. Sci.* **2018**, *11* (5), 1062−1176.

(4) Choi, S.; Drese, J. H.; Jones, C. W. Adsorbent Materials for Carbon Dioxide Capture from Large Anthropogenic Point Sources. *ChemSusChem* **2009**, *2* (9), 796−854.

(5) Rochelle, G. T. Amine scrubbing for CO2 capture. *Science* **2009**, *325* (5948), 1652−1654.




DOI: 10.1021/acssuschemeng.9b02035
ACS Sustainable Chem. Eng. 2019, 7, 12464−12473

(6) Mota-Martinez, M. T.; Hallett, J. P.; Mac Dowell, N. Solvent selection and design for CO2 capture - how we might have been missing the point. *Sustain. Energy Fuels* **2017**, *1* (10), 2078−2090.
(7) Leal, O.; Bolívar, C.; Ovalles, C.; García, J. J.; Espidel, Y. Reversible adsorption of carbon dioxide on amine surface-bonded silica gel. *Inorg. Chim. Acta* **1995**, *240* (1), 183−189.
(8) Pennline, H. W.; Luebke, D. R.; Jones, K. L.; Myers, C. R.; Morsi, B. I.; Heintz, Y. J.; Ilconich, J. B. Progress in carbon dioxide capture and separation research for gasification-based power generation point sources. *Fuel Process. Technol.* **2008**, *89* (9), 897−907.
(9) Mafra, L.; Ćendak, T.; Schneider, S.; Wiper, P. V.; Pires, J.; Gomes, J. R. B.; Pinto, M. L. Structure of Chemisorbed CO2 Species in Amine-Functionalized Mesoporous Silicas Studied by Solid-State NMR and Computer Modeling. *J. Am. Chem. Soc.* **2017**, *139* (1), 389−408.
(10) Presser, V.; McDonough, J.; Yeon, S.-H.; Gogotsi, Y. Effect of pore size on carbon dioxide sorption by carbide derived carbon. *Energy Environ. Sci.* **2011**, *4* (8), 3059−3066.
(11) Patel, H. A.; Byun, J.; Yavuz, C. T. Carbon Dioxide Capture Adsorbents: Chemistry and Methods. *ChemSusChem* **2017**, *10* (7), 1303−1317.
(12) Sircar, S.; Golden, T.C.; Rao, M.B. Activated carbon for gas separation and storage. *Carbon* **1996**, *34* (1), 1−12.
(13) Ben-Mansour, R.; Habib, M. A.; Bamidele, O. E.; Basha, M.; Qasem, N. A. A.; Peedikakkal, A.; Laoui, T.; Ali, M. Carbon capture by physical adsorption: Materials, experimental investigations and numerical modeling and simulations - A review. *Appl. Energy* **2016**, *161*, 225−255.
(14) Wang, J. Y.; Huang, L.; Yang, R. Y.; Zhang, Z.; Wu, J. W.; Gao, Y. S.; Wang, Q.; O'Hare, D.; Zhong, Z. Y. Recent advances in solid sorbents for CO2 capture and new development trends. *Energy Environ. Sci.* **2014**, *7* (11), 3478−3518.
(15) Rashidi, N. A.; Yusup, S. An overview of activated carbons utilization for the post-combustion carbon dioxide capture. *J. CO2 Util.* **2016**, *13*, 1−16.
(16) Ding, M.; Flaig, R. W.; Jiang, H.-L.; Yaghi, O. M. Carbon capture and conversion using metal−organic frameworks and MOF-based materials. *Chem. Soc. Rev.* **2019**, *48* (10), 2783−2828.
(17) Cinke, M.; Li, J.; Bauschlicher, C. W.; Ricca, A.; Meyyappan, M. CO2 adsorption in single-walled carbon nanotubes. *Chem. Phys. Lett.* **2003**, *376* (5), 761−766.
(18) Zhou, J.; Li, Z.; Xing, W.; Shen, H.; Bi, X.; Zhu, T.; Qiu, Z.; Zhuo, S. A New Approach to Tuning Carbon Ultramicropore Size at Sub-Angstrom Level for Maximizing Specific Capacitance and CO2 Uptake. *Adv. Funct. Mater.* **2016**, *26* (44), 7955−7964.
(19) Alhwaige, A. A.; Agag, T.; Ishida, H.; Qutubuddin, S. Biobased chitosan hybrid aerogels with superior adsorption: Role of graphene oxide in CO2 capture. *RSC Adv.* **2013**, *3* (36), 16011−16020.
(20) Zhang, Z.; Luo, D.; Lui, G.; Li, G.; Jiang, G.; Cano, Z. P.; Deng, Y.-P.; Du, X.; Yin, S.; Chen, Y.; Zhang, M.; Yan, Z.; Chen, Z. In-situ ion-activated carbon nanospheres with tunable ultramicroporosity for superior CO2 capture. *Carbon* **2019**, *143*, 531−541.
(21) Wickramaratne, N. P.; Xu, J.; Wang, M.; Zhu, L.; Dai, L.; Jaroniec, M. Nitrogen Enriched Porous Carbon Spheres: Attractive Materials for Supercapacitor Electrodes and CO2 Adsorption. *Chem. Mater.* **2014**, *26* (9), 2820−2828.
(22) Maroto-Valer, M. M.; Tang, Z.; Zhang, Y. CO2 capture by activated and impregnated anthracites. *Fuel Process. Technol.* **2005**, *86* (14), 1487−1502.
(23) Zhang, Z.; Xu, M.; Wang, H.; Li, Z. Enhancement of CO2 adsorption on high surface area activated carbon modified by N2, H2 and ammonia. *Chem. Eng. J.* **2010**, *160* (2), 571−577.
(24) Silvestre-Albero, A.; Silvestre-Albero, J.; Martínez-Escandell, M.; Rodríguez-Reinoso, F. Micro/Mesoporous Activated Carbons Derived from Polyaniline: Promising Candidates for CO2 Adsorption. *Ind. Eng. Chem. Res.* **2014**, *53* (40), 15398−15405.
(25) Khalili, S.; Khoshandam, B.; Jahanshahi, M. Synthesis of activated carbon/polyaniline nanocomposites for enhanced CO2 adsorption. *RSC Adv.* **2016**, *6* (42), 35692−35704.
(26) Peyravi, M. Synthesis of nitrogen doped activated carbon/polyaniline material for CO2 adsorption. *Polym. Adv. Technol.* **2018**, *29* (1), 319−328.
(27) Qian, M.; Wang, Z.; Li, Z.; Xu, J.; Sun, P.; Lin, J.; Lin, T.; Huang, F. Sol-gel assisted chemical activation for nitrogen doped porous carbon. *Microporous Mesoporous Mater.* **2019**, *286*, 18−24.
(28) Alfe, M.; Ammendola, P.; Gargiulo, V.; Raganati, F.; Chirone, R. Magnetite loaded carbon fine particles as low-cost CO2 adsorbent in a sound assisted fluidized bed. *Proc. Combust. Inst.* **2015**, *35* (3), 2801−2809.
(29) Mishra, A. K.; Ramaprabhu, S. Nanostructured polyaniline decorated graphene sheets for reversible CO2 capture. *J. Mater. Chem.* **2012**, *22*, 3708−3712.
(30) Mishra, A. K.; Ramaprabhu, S. Enhanced CO2 capture in Fe3O4-graphene nanocomposite by physicochemical adsorption. *J. Appl. Phys.* **2014**, *116* (6), 064306.
(31) Kumar Mishra, A.; Ramaprabhu, S. Polyaniline/multiwalled carbon nanotubes nanocomposite-an excellent reversible CO2 capture candidate. *RSC Adv.* **2012**, *2* (5), 1746−1750.
(32) Li, X. F.; Jin, Y. K.; Xue, Q. Z.; Zhu, L.; Xing, W.; Zheng, H. X.; Liu, Z. L. Ultra-high selective capture of CO2 on one-sided N-doped carbon nanoscrolls. *J. CO2 Util.* **2017**, *18*, 275−282.
(33) Alghamdi, A. A.; Alshahrani, F. A.; Khdary, H. N.; Alharthi, A. F.; Alattas, A. H.; Adil, F. S. Enhanced CO2 Adsorption by Nitrogen-Doped Graphene Oxide Sheets (N-GOs) Prepared by Employing Polymeric Precursors. *Materials* **2018**, *11* (4), 578.
(34) Mishra, A. K.; Ramaprabhu, S. Carbon dioxide adsorption in graphene sheets. *AIP Adv.* **2011**, *1* (3), 032152.
(35) Hidalgo, R. S.; López-Díaz, D.; Velázquez, M. M. Graphene Oxide Thin Films: Influence of Chemical Structure and Deposition Methodology. *Langmuir* **2015**, *31* (9), 2697−2705.
(36) López-Díaz, D.; López Holgado, M.; García-Fierro, J. L.; Velázquez, M. M. Evolution of the Raman Spectrum with the Chemical Composition of Graphene Oxide. *J. Phys. Chem. C* **2017**, *121* (37), 20489−20497.
(37) Claramunt, S.; Varea, A.; López-Díaz, D.; Velázquez, M. M.; Cornet, A.; Cirera, A. The Importance of Interbands on the Interpretation of the Raman Spectrum of Graphene Oxide. *J. Phys. Chem. C* **2015**, *119* (18), 10123−10129.
(38) López-Díaz, D.; Mercedes Velázquez, M.; Blanco de La Torre, S.; Pérez-Pisonero, A.; Trujillano, R.; Fierro, J. L. G.; Claramunt, S.; Cirera, A. The Role of Oxidative Debris on Graphene Oxide Films. *ChemPhysChem* **2013**, *14* (17), 4002−4009.
(39) Christian Kemp, K; Chandra, V.; Saleh, M.; Kim, K. S Reversible CO2 adsorption by an activated nitrogen doped graphene/polyaniline material. *Nanotechnology* **2013**, *24* (23), 235703.
(40) Udovic, T. J.; Dumesic, J. A. Adsorptive properties of magnetite surfaces as studied by temperature-programmed desorption: Studies of O2, NO, CO2, and CO adsorption. *J. Catal.* **1984**, *89* (2), 314−326.
(41) Hakim, A.; Marliza, T. S.; Abu Tahari, N. M.; Wan Isahak, R. W. N.; Yusop, R. M.; Mohamed Hisham, W. M.; Yarmo, A. M. Studies on CO2 Adsorption and Desorption Properties from Various Types of Iron Oxides (FeO, Fe2O3, and Fe3O4). *Ind. Eng. Chem. Res.* **2016**, *55* (29), 7888−7897.
(42) Tamaura, Y.; Nishizawa, K. i. CO2 decomposition into C and conversion into CH4 using the H2-reduced magnetite. *Energy Convers. Manage.* **1992**, *33* (5), 573−577.
(43) Wang, H.; Hao, Q.; Yang, X.; Lu, L.; Wang, X. Graphene oxide doped polyaniline for supercapacitors. *Electrochem. Commun.* **2009**, *11* (6), 1158−1161.
(44) Mishra, A. K.; Ramaprabhu, S. Magnetite Decorated Multi-walled Carbon Nanotube Based Supercapacitor for Arsenic Removal and Desalination of Seawater. *J. Phys. Chem. C* **2010**, *114* (6), 2583−2590.


DOI: 10.1021/acssuschemeng.9b02035
*ACS Sustainable Chem. Eng.* 2019, 7, 12464−12473

(45) Dubinin, M. M. Adsorption properties and microporous structures of carbonaceous adsorbents. *Carbon* **1987**, *25* (5), 593–598.
(46) Moya, C.; Palomar, J.; Gonzalez-Miquel, M.; Bedia, J.; Rodriguez, F. Diffusion Coefficients of CO2 in Ionic Liquids Estimated by Gravimetry. *Ind. Eng. Chem. Res.* **2014**, *53* (35), 13782–13789.
(47) Wang, L.-y.; Xu, Y.-l.; Li, Z.-d.; Wei, Y.-n.; Wei, J.-p. CO2/CH4 and H2S/CO2 Selectivity by Ionic Liquids in Natural Gas Sweetening. *Energy Fuels* **2018**, *32* (1), 10–23.
(48) Ho, Y. S.; McKay, G. Pseudo-second order model for sorption processes. *Process Biochem.* **1999**, *34* (5), 451–465.
(49) Azizian, S. A novel and simple method for finding the heterogeneity of adsorbents on the basis of adsorption kinetic data. *J. Colloid Interface Sci.* **2006**, *302* (1), 76–81.
(50) Singh, V. K.; Kumar, E. A. Comparative Studies on CO2 Adsorption Kinetics by Solid Adsorbents. In *5th International Conference on Advances in Energy Research*; Banerjee, R., Bandyopadhyay, S., Kavaipatti, B., Mitra, S., Eds.; Elsevier Science Bv: Amsterdam, 2016; Vol. *90*, pp 316–325.
(51) Hontoria-Lucas, C.; López-Peinado, A. J.; López-González, J. d. D.; Rojas-Cervantes, M. L.; Martín-Aranda, R. M. Study of oxygen-containing groups in a series of graphite oxides: Physical and chemical characterization. *Carbon* **1995**, *33* (11), 1585–1592.
(52) Martín-García, B.; Velázquez, M. M.; Rossella, F.; Bellani, V.; Diez, E.; García Fierro, J. L.; Pérez-Hernández, J. A.; Hernández-Toro, J.; Claramunt, S.; Cirera, A. Functionalization of Reduced Graphite Oxide Sheets with a Zwitterionic Surfactant. *ChemPhysChem* **2012**, *13* (16), 3682–3690.
(53) Wang, H.; Hao, Q.; Yang, X.; Lu, L.; Wang, X. Effect of Graphene Oxide on the Properties of Its Composite with Polyaniline. *ACS Appl. Mater. Interfaces* **2010**, *2* (3), 821–828.
(54) Monkman, A. P.; Stevens, G. C.; Bloor, D. X-ray photoelectron spectroscopic investigations of the chain structure anddoping mechanisms in polyaniline. *J. Phys. D: Appl. Phys.* **1991**, *24* (5), 738.
(55) Trchova, M.; Stejskal, J. Polyaniline: The infrared spectroscopy of conducting polymer nanotubes (IUPAC Technical Report). *Pure Appl. Chem.* **2011**, *83* (10), 1803–1817.
(56) Boyer, M. I.; Quillard, S.; Rebourt, E.; Louarn, G.; Buisson, J. P.; Monkman, A.; Lefrant, S. Vibrational Analysis of Polyaniline: A Model Compound Approach. *J. Phys. Chem. B* **1998**, *102* (38), 7382–7392.
(57) Ćirić-Marjanović, G.; Dragičević, L.; Milojević, M.; Mojović, M.; Mentus, S.; Dojčinović, B.; Marjanović, B.; Stejskal, J. Synthesis and Characterization of Self-Assembled Polyaniline Nanotubes/Silica Nanocomposites. *J. Phys. Chem. B* **2009**, *113* (20), 7116–7127.
(58) Mishra, A. K.; Ramaprabhu, S. Functionalized Graphene-Based Nanocomposites for Supercapacitor Application. *J. Phys. Chem. C* **2011**, *115* (29), 14006–14013.
(59) Jeong, H.-K.; Lee, Y. P.; Jin, M. H.; Kim, E. S.; Bae, J. J.; Lee, Y. H. Thermal stability of graphite oxide. *Chem. Phys. Lett.* **2009**, *470* (4–6), 255–258.
(60) Muzyka, R.; Kwoka, M.; Smędowski, Ł.; Díez, N.; Gryglewicz, G. Oxidation of graphite by different modified Hummers methods. *New Carbon Materials* **2017**, *32* (1), 15–20.
(61) Varela-Rizo, H.; Rodriguez-Pastor, I.; Merino, C.; Terrones, M.; Martin-Gullon, I. Graphene oxide nanoplatelets of different crystallinity synthesized from helical-ribbon carbon nanofibers and multiwall carbon nanotubes. *J. Mater. Res.* **2011**, *26* (20), 2632–2641.
(62) Gui, D.; Liu, C.; Chen, F.; Liu, J. Preparation of polyaniline/graphene oxide nanocomposite for the application of supercapacitor. *Appl. Surf. Sci.* **2014**, *307*, 172–177.
(63) Yang, D.; Velamakanni, A.; Bozoklu, G.; Park, S.; Stoller, M.; Piner, R. D.; Stankovich, S.; Jung, I.; Field, D. A.; Ventrice, C. A., Jr; Ruoff, R. S. Chemical analysis of graphene oxide films after heat and chemical treatments by X-ray photoelectron and Micro-Raman spectroscopy. *Carbon* **2009**, *47* (1), 145–152.
(64) Sun, H.; Cao, L.; Lu, L. Magnetite/reduced graphene oxide nanocomposites: One step solvothermal synthesis and use as a novel platform for removal of dye pollutants. *Nano Res.* **2011**, *4* (6), 550–562.
(65) Yamashita, T.; Hayes, P. Analysis of XPS spectra of Fe2+ and Fe3+ ions in oxide materials. *Appl. Surf. Sci.* **2008**, *254* (8), 2441–2449.
(66) Ke, Q.; Tang, C.; Liu, Y.; Liu, H.; Wang, J. Intercalating graphene with clusters of Fe 3 O 4 nanocrystals for electrochemical supercapacitors. *Materials Research Express* **2014**, *1* (2), 025015.
(67) Wang, W.; Tang, B.; Ju, B.; Gao, Z.; Xiu, J.; Zhang, S. Fe3O4-functionalized graphene nanosheet embedded phase change material composites: efficient magnetic- and sunlight-driven energy conversion and storage. *J. Mater. Chem. A* **2017**, *5* (3), 958–968.
(68) Deng, J.-H.; Zhang, X.-R.; Zeng, G.-M.; Gong, J.-L.; Niu, Q.-Y.; Liang, J. Simultaneous removal of Cd(II) and ionic dyes from aqueous solution using magnetic graphene oxide nanocomposite as an adsorbent. *Chem. Eng. J.* **2013**, *226*, 189–200.
(69) Mishra, A. K.; Ramaprabhu, S. Nano magnetite decorated multiwalled carbon nanotubes: a robust nanomaterial for enhanced carbon dioxide adsorption. *Energy Environ. Sci.* **2011**, *4* (3), 889–895.
(70) Mahdavi, M.; Ahmad, M.; Haron, M.; Namvar, F.; Nadi, B.; Rahman, M.; Amin, J. Synthesis, Surface Modification and Characterisation of Biocompatible Magnetic Iron Oxide Nanoparticles for Biomedical Applications. *Molecules* **2013**, *18* (7), 7533.
(71) Arne, T. Functional Materials: From Hard to Soft Porous Frameworks. *Angew. Chem., Int. Ed.* **2010**, *49* (45), 8328–8344.
(72) Chaoui, N.; Trunk, M.; Dawson, R.; Schmidt, J.; Thomas, A. Trends and challenges for microporous polymers. *Chem. Soc. Rev.* **2017**, *46* (11), 3302–3321.
(73) Nguyen, C.; Do, D. D. The Dubinin-Radushkevich equation and the underlying microscopic adsorption description. *Carbon* **2001**, *39* (9), 1327–1336.
(74) Wei, X.; Jiang, X.; Wei, J.; Gao, S. Functional Groups and Pore Size Distribution Do Matter to Hierarchically Porous Carbons as High-Rate-Performance Supercapacitors. *Chem. Mater.* **2016**, *28* (2), 445–458.
(75) Lee, M.-S.; Park, M.; Kim, H. Y.; Park, S.-J. Effects of Microporosity and Surface Chemistry on Separation Performances of N-Containing Pitch-Based Activated Carbons for CO2/N-2 Binary Mixture. *Sci. Rep.* **2016**, *6*, 23224.


DOI: 10.1021/acssuschemeng.9b02035
*ACS Sustainable Chem. Eng.* 2019, 7, 12464–12473